



Article

# Quantum Memristors in Frequency-Entangled Optical Fields

Tasio Gonzalez-Raya <sup>1,\*</sup>, Joseph M. Lukens <sup>2</sup> , Lucas C. Céleri <sup>1,3</sup> and Mikel Sanz <sup>1,\*</sup> 

<sup>1</sup> Department of Physical Chemistry, University of the Basque Country UPV/EHU, Apartado 644, 48080 Bilbao, Spain; lcceleri@gmail.com

<sup>2</sup> Quantum Information Science Group, Oak Ridge National Laboratory, Oak Ridge, TN 37831, USA; lukensjm@ornl.gov

<sup>3</sup> Institute of Physics, Federal University of Goiás, 74.690-900 Goiânia, Goiás, Brazil

\* Correspondence: tasio.gonzalez@ehu.eus (T.G.-R.); mikel.sanz@ehu.eus (M.S.)

Received: 24 December 2019; Accepted: 5 February 2020; Published: 14 February 2020



**Abstract:** A quantum memristor is a passive resistive circuit element with memory, engineered in a given quantum platform. It can be represented by a quantum system coupled to a dissipative environment, in which a system–bath coupling is mediated through a weak measurement scheme and classical feedback on the system. In quantum photonics, such a device can be designed from a beam splitter with tunable reflectivity, which is modified depending on the results of measurements in one of the outgoing beams. Here, we show that a similar implementation can be achieved with frequency-entangled optical fields and a frequency mixer that, working similarly to a beam splitter, produces state superpositions. We show that the characteristic hysteretic behavior of memristors can be reproduced when analyzing the response of the system with respect to the control, for different experimentally attainable states. Since memory effects in memristors can be exploited for classical and neuromorphic computation, the results presented in this work could be a building block for constructing quantum neural networks in quantum photonics, when scaling up.

**Keywords:** quantum memristors; memristive systems; quantum photonics; quantum neural networks

## 1. Introduction

Memory circuit elements are poised to introduce a new paradigm in both classical and quantum computation [1–5]. Due to their dependence on previous dynamics, it seems fitting to exploit their passive storage capabilities for enhancement of information processing and for neuromorphic computing tasks. One of these memory circuit elements is called the memristor [6]. It describes a resistive element of an electric circuit that has memory, with a changing resistance whose instantaneous value depends on the history of signals that have crossed the device. This information is codified in the internal variable of the memristor,  $\mu$ , introducing a state-dependent Ohm's law

$$I(t) = G(\mu(t))V(t), \quad (1)$$

$$\dot{\mu}(t) = f(\mu(t), V(t)), \quad (2)$$

for a voltage-controlled memristor. The dynamic behavior is given by  $f(\mu(t), V(t))$ , and is manifest in the state-dependent conductance  $G(\mu(t)) > 0$ . Attempting to solve Equation (2) requires time integration over the past of the control signal. This means that the current response given by the voltage-controlled memristor described in Equation (1) depends, through  $G(\mu)$ , on previous values of the control voltage, as well as on the present one. Thus, a memristor that undergoes a periodic control signal will display a hysteresis loop when plotting the response versus the control signal (current vs.

voltage). The slope of this curve is identified with the resistance of the device, and the area enclosed by it is associated with memory effects [7].

This behavior can be described by Kubo's response theory [8], but it was Chua who, in 1971, coined the term "memristor" and described it as an independent element in an electric circuit [9]. It took almost 40 years until such a device was engineered, taking advantage of solid-state electronic and ionic transport properties in nanoscale structures [10]. On this research front, new ways to engineer and optimize memristors are being proposed [11]. Apart from the advantages of using these devices for computation [12] (such as energy efficiency [13], compared to transistor-based computers), memristors can be also used in machine learning schemes [14,15]. The relevance of the memristor lies in its ubiquitous presence in models which describe natural processes, especially those involving biological systems. For example, memristors inherently describe voltage-dependent ion-channel conductances in the axon membrane in neurons, present in the Hodgkin–Huxley model [16,17].

Due to the inherent linearity of quantum mechanics, it is not straightforward to describe a dissipative non-linear memory element, such as the memristor, in the quantum realm, since nonlinearities usually lead to the violation of fundamental quantum principles, such as no-cloning theorem. Nonetheless, the challenge was already constructively addressed in Ref. [18]. This consists of a harmonic oscillator coupled to a dissipative environment, where the coupling is changed based on the results of a weak measurement scheme with classical feedback. As a result of the development of quantum platforms in recent years, and their improvement in controllability and scalability, different constructions of a quantum memristor in such platforms have been presented. There is a proposal for implementing it in superconducting circuits [7], exploiting memory effects that naturally arise in Josephson junctions. The second proposal is based on integrated photonics [19]: a Mach–Zehnder interferometer can behave as a beam splitter with a tunable reflectivity by introducing a phase in one of the beams, which can be manipulated to study the system as a quantum memristor subject to different quantum state inputs.

In this article, we study a different implementation of a quantum memristor in a quantum photonics setup. Employing beam splitters for frequency-codified quantum states [20], we explore a new implementation in which the information is codified in frequency-entangled optical fields. We engineer the elements which constitute a quantum memristor, namely a tunable dissipative element, a weak-measurement scheme, and classical feedback. We find that the characteristic  $I$ – $V$  curve displays hysteresis loops when subjecting the system to different quantum state inputs. The aim of this work is to establish a building block for memristor-based quantum photonic neural networks with frequency-codified state inputs, which could ultimately have applications in quantum machine learning and quantum neural networks [21,22].

## 2. Results

A memristor can be implemented in quantum optics by means of a beam splitter with a tunable reflectivity. The required non-Markovian dynamics is achieved by inserting a detector in one of the outcomes of the beam splitter (the environment) and, via a feedback mechanism, changing the reflectivity of the beam splitter. In this way, the coupling between the system (second beam splitter output) and the environment will depend on the previous history of the reflectivity, thus building up memory effects. We present a sketch of this device in Figure 1.

Formally, a beam splitter with transmissivity  $\eta = \cos \phi$  is described by the operator

$$\hat{U}_{BS}(\phi, \varphi) = e^{\phi(a_0^\dagger a_1 e^{i\varphi} - a_0 a_1^\dagger e^{-i\varphi})}, \quad (3)$$

where  $a_0$  and  $a_1$  are the mode operators for the signal and ancillary signals, respectively, while  $\varphi$  stands for an arbitrary fixed phase. The action of the beam splitter on the input modes  $\mathbf{a} = (a_0 \ a_1)^T$  can then be expressed via a  $2 \times 2$  matrix  $B$ ,

$$\mathbf{b} = B(\phi, \varphi)\mathbf{a}, \quad (4)$$

with  $\mathbf{b} = (b_0 \ b_1)^T$  being the vector containing the output signal mode  $b_0$  and the environmental mode  $b_1$ . The goal of the feedback system  $\mathcal{F}$  is to control the value of  $\phi$  based on the result of the measurement performed on the environment, thus generating time correlations, the characteristic feature of non-Markovianity, at the output mode  $b_0$ .

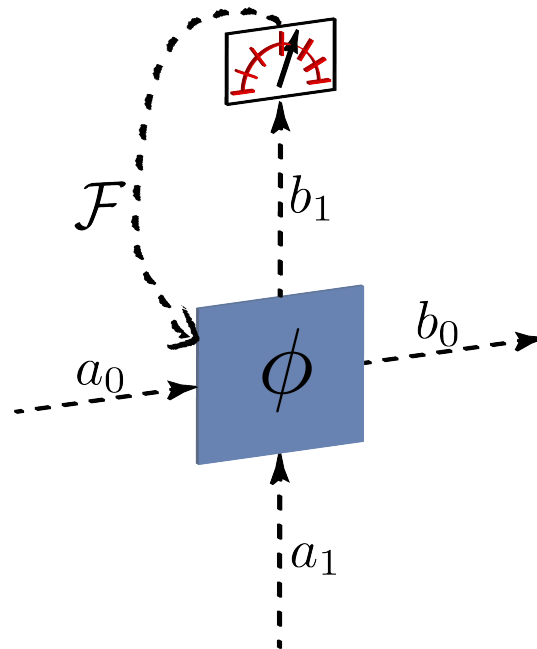


**Figure 1.** Graphical representation of a photonic quantum memristor. This consists of a beam splitter with tunable reflectivity, a measurement scheme, and a classical feedback system  $\mathcal{F}$ .

We consider the memristor based on a frequency beam splitter, which is a Hadamard gate acting on the frequency degree of freedom of the input, a central element for universal frequency-based quantum computation [23]. Recent research has explored implementing unitary operations, such as that in Equation (3), in time- or frequency-based photonic Hilbert spaces as alternatives to more traditional path encoding approaches. In the frequency-comb-based paradigms, in particular those in Refs. [23,24], quantum information is carried by photons in discrete modes ( $a_n$  or  $b_n$ ), distinguished by index  $n \in \mathbb{Z}$  within an equispaced comb defined by frequencies  $\nu_n = \nu_0 + n\Delta\nu$ . Such an encoding format proves intriguing given its synergy with fiber-optic networks, applicability to frequency-disparate quantum interconnects, high parallelizability, and compatibility with on-chip photon sources [25]. However, implementing coherent operations between frequency bins forms a challenging prospect, typically requiring optical nonlinearities mediated by strong pump fields [26,27]. However, in 2017, based on electro-optic phase modulators (EOMs) and Fourier-transform pulse shapers, an alternative approach was proposed [23]. By cascading EOMs and pulse shapers in an alternating sequence, in principle, any frequency-bin unitary can be realized with favorable resource scaling. As these operations are optically linear and precisely controllable, multiple demonstrations have followed this initial proposal, completing the basic pieces of a universal quantum gate set [28].

The 50/50 frequency beam splitter (or Hadamard gate) was the focus of the first experiment in this model [20], where it was found that—even when restricting to simple, but practically convenient, sinewave-only EOM patterns—a three-element EOM/pulse shaper/EOM sequence was able to realize a high-fidelity frequency-bin Hadamard with only a slight (2.4%) reduction in success probability. Further investigation showed that this particular configuration was readily tunable as well; keeping the EOM modulation fixed and modifying only the phase applied by the pulse shaper, the frequency beam splitter reflectivity can be adjusted between 0% and 50%, a feature subsequently exploited for Hong–Ou–Mandel interference in the frequency domain [29]. Importantly, this tunability is precisely

the prerequisite for a quantum memristor of the form of Figure 1, thus motivating our detailed exploration of the frequency-bin beam splitter here.

Figure 2 furnishes a possible experimental setup for a frequency-bin memristor. Input spectral modes  $a_0$  and  $a_1$  are combined into a single fiber where they experience temporal phase modulation at amplitude  $\Theta$  and cyclic frequency  $\Delta\nu$ , followed by a pulse shaper which applies a phase shift  $\phi$  to the modes  $n \geq 1$  (including those outside of the two-dimensional space of  $n \in \{0, 1\}$ ). A second EOM, driven at the same amplitude as the first, but exactly out of phase, concludes the frequency beam splitter. Then, the output  $b_1$  is extracted and measured, the results of which are used to update the pulse shaper phase shift  $\phi$ .

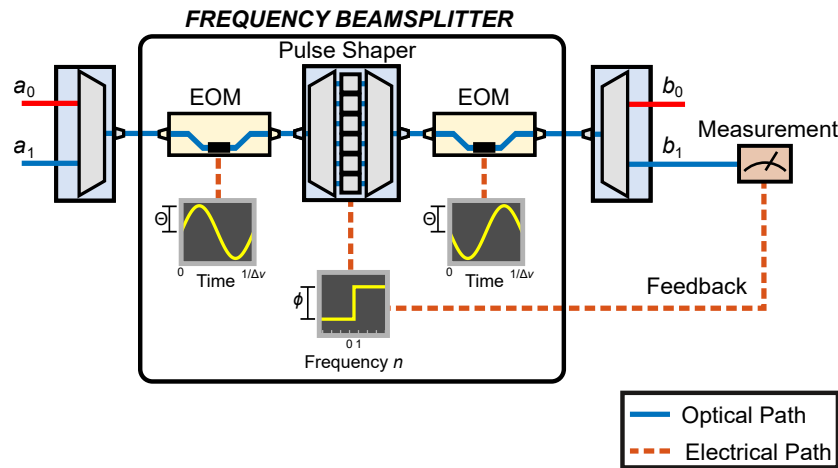


Figure 2. Experimental setup showing a memristor based on the frequency beam splitter.

Mathematically, each EOM multiplies the input field in the time domain by  $\exp[\pm i\Theta \sin(2\pi\Delta\nu t)]$ , for the first and second EOM, respectively. Using a Fourier series expansion, this transformation on frequency-bin operators can be modeled as  $b_m = \sum_n c_{m-n} a_n$  with  $c_n = (\mp)^n J_n(\Theta)$ , with  $J_n(\cdot)$  denoting the  $n$ th order Bessel function of the first kind. The pulse shaper sandwiched between these two EOMs applies the phase  $\phi$  to all bins  $n \geq 1$  and zero to all  $n \leq 0$ . Cascading these three operations, then, we arrive at the following matrix elements connecting the input and output modes of the beam splitter ( $n \in \{0, 1\}$ ).

$$\begin{aligned}
 B_{00} &= e^{i\frac{\phi}{2}} \left[ \cos \frac{\phi}{2} - iJ_0^2(\Theta) \sin \frac{\phi}{2} \right], \\
 B_{01} &= -2i \left[ \sum_{k=1}^{\infty} J_k(\Theta) J_{k-1}(\Theta) \right] e^{i\frac{\phi}{2}} \sin \frac{\phi}{2}, \\
 B_{10} &= -2i \left[ \sum_{k=1}^{\infty} J_k(\Theta) J_{k-1}(\Theta) \right] e^{i\frac{\phi}{2}} \sin \frac{\phi}{2}, \\
 B_{11} &= e^{i\frac{\phi}{2}} \left[ \cos \frac{\phi}{2} + iJ_0^2(\Theta) \sin \frac{\phi}{2} \right].
 \end{aligned} \tag{5}$$

The 50/50 beam splitter corresponds to the case  $\Theta = 0.8169$  and  $\phi = \pi$ ; under these settings, the  $2 \times 2$  matrix matches the Hadamard operation with fidelity  $\mathcal{F} = 0.9999$ , up to an overall scaling factor that makes the matrix slightly non-unitary due to residual photon scattering into the frequency

bins outside of the two-dimensional space [20]. This deviation from unitarity at  $\phi = \pi$  can be quantified by  $B^\dagger(\pi, \Theta)B(\pi, \Theta) = f(\Theta) \cdot \mathbb{I}$ , where

$$f(\Theta) = J_0^4(\Theta) + 4 \left[ \sum_{k=1}^{\infty} J_k(\Theta)J_{k-1}(\Theta) \right]^2. \tag{6}$$

Figure 3 shows the region where  $f(\Theta)$  is close to the value of one required for unitarity;  $f(0.8169) = 0.9760$ , which corresponds to the success probability  $\mathcal{P}$  defined in Ref. [20]. This solution can be viewed as the “most unitary” high-fidelity ( $\mathcal{F} \geq 0.9999$ ) approximation to the Hadamard with two EOMs, one pulse shaper, and single-tone electro-optic modulation. We do note, however, that a fully unitary Hadamard could be realized either by considering arbitrary modulation patterns or adding components; the current settings represent an experimentally-valuable compromise between performance and complexity. Thus, with  $\Theta$  fixed at 0.8169, adjusting  $\phi$ , enables tuning of the frequency-bin reflectivity ( $|B_{01}|^2 = |B_{10}|^2$ ) and transmissivity ( $|B_{00}|^2 = |B_{11}|^2$ ) as needed for the memristor.

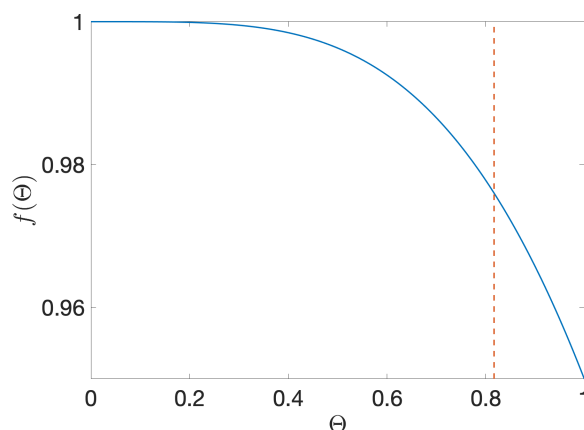


**Figure 3.** Unitarity of the matrix  $B$  for any value of the phase  $\phi$ . The dashed vertical line shows the value  $\Theta = 0.8169$ , which, together with  $\phi = \pi$ , corresponds to the experimental setup for the realization of the Hadamard gate on such a device.

In the measurement and feedback scheme, we aim at modifying the phase  $\phi$  appearing in Equation (5) depending on the result of the measurement at the environment output of the beam splitter—the other output functions as the response signal of the memristor. The measurement scheme is based on photon number measurements, as illustrated in Figure 4.

Each  $\mu_i$  represents the result of an experiment with a fixed phase, after which we obtain an average of the number of photons in the environment output of the beam splitter, corresponding to the reflected beam. The average number of photons in the outgoing beams, depending on a certain observable of the input state, such as the quadrature  $\langle x_0^{\text{in}} \rangle$ , are

$$\begin{aligned} \langle n_0^{\text{out}} \rangle &= f_0(\phi, \langle x_0^{\text{in}} \rangle), \\ \langle n_1^{\text{out}} \rangle &= f_1(\phi, \langle x_0^{\text{in}} \rangle). \end{aligned} \tag{7}$$

$\phi$  is modified according to the latter, following a dynamic equation

$$\dot{\phi} = g(\phi, \langle n_1^{\text{out}} \rangle), \tag{8}$$

which we are free to choose. For illustrative purposes, we propose oscillating input states, for example  $\langle x_0^{\text{in}} \rangle = \langle x_0^{\text{in}} \rangle_{\text{max}} \cos \omega t$ , where  $\omega$  is a free parameter that we can choose to optimize the correlations and memory persistence in the system.

The result of the measurement process corresponds to a time average of the number of photons, reflected in the beam splitter, that are detected, with fixed  $\phi$ , where  $\tau_k$  defines the duration of one complete experiment  $k$ . The result of each experiment is then used to update  $\phi$ , which is changed for time slices between experiments. However, the global change of  $\phi$  occurs in a timescale given by  $\omega^{-1}$ , whereas the duration of each experiment is  $\tau_k$ , thus, to have a continuous dynamic equation for the update of  $\phi$ , we are assuming  $\tau_k \omega \ll 1$ . Since we are assuming high-precision control of the internal variable in our system, the effect of the memristor stochastic catastrophe is negligible [30].

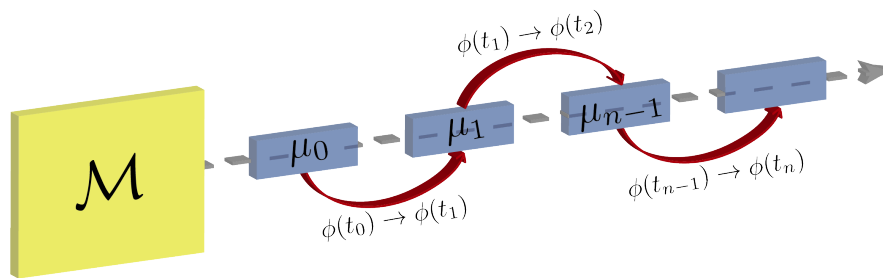


**Figure 4.** Graphical representation of the measurement schemes that lead to the evolution of the memory variable. Photon number measurements are performed on the environment, followed by a modification of phase  $\phi$  depending on the averaged value of these measurements. In this figure,  $\mathcal{M}$  represents the quantum memristor. Each individual experiment occurring at time  $t_k$ , with a fixed phase  $\phi(t_k)$ , is labeled by  $\mu_k$ , after which a value for the average number of output photons is obtained. This value is used to change the value of  $\phi$ , from  $\phi(t_k)$  to  $\phi(t_{k+1})$ .

The hysteresis loop area, characteristic of the memristor’s non-Markovian behavior, can be understood as a memory quantifier. Our goal here is to optimize the feedback process to obtain maximum time correlation at the output signal, since this quantity will be related to the memory persistence in the system. This is crucial, especially when designing a neural network based on quantum memristors, where we would look to minimize decoherence in order to take advantage of quantum effects. This optimization will also allow us to study the persistence of the memory effects in the system, affected as well by the feedback mechanism.

Now, let us look into the effect of this device on different initial states, analyzing their hysteretic response.

### 2.1. Coherent States

The two-mode coherent states are given by

$$|\alpha_{\omega_0}, \beta_{\omega_1}\rangle = e^{-(|\alpha|^2 + |\beta|^2)/2} \sum_{n,m=0}^{\infty} \frac{\alpha^n \beta^m}{\sqrt{n!m!}} (a_{\omega_0}^\dagger)^n (a_{\omega_1}^\dagger)^m |0, 0\rangle, \tag{9}$$

where  $\alpha$  and  $\beta$  are complex numbers that can be experimentally tuned.

Recall that a coherent state  $|\alpha\rangle$  can be defined by the displacement operator  $D(\alpha) = e^{\alpha a^\dagger - \bar{\alpha} a}$  acting on the vacuum,  $|\alpha\rangle = D(\alpha)|0\rangle$ . Using the equality

$$e^A B e^{-A} = \sum_{k=0}^{\infty} \frac{1}{k!} [A, [A, \dots, [A, B] \dots]] \tag{10}$$

derived from the Baker–Campbell–Hausdorff transformation for any two operators  $A, B$ , we arrive at

$$D(\alpha)^\dagger a D(\alpha) = a + \alpha. \tag{11}$$

By applying displacement operators  $D(\alpha)$ ,  $D(\beta)$  on the first and second beams, respectively, we achieve the following transformation

$$\begin{pmatrix} a_0 \\ a_1 \end{pmatrix} \longrightarrow \begin{pmatrix} D^\dagger(\alpha)a_0D(\alpha) \\ D^\dagger(\beta)a_1D(\beta) \end{pmatrix} = \begin{pmatrix} a_0 + \alpha \\ a_1 + \beta \end{pmatrix} \tag{12}$$

and these modes are the input to the beam splitter. Then, we compute

$$\begin{pmatrix} b_0 \\ b_1 \end{pmatrix}_{\text{coh}} = B(\phi) \begin{pmatrix} a_0 + \alpha \\ a_1 + \beta \end{pmatrix} = \begin{pmatrix} B_{00}(a_0 + \alpha) + B_{01}(a_1 + \beta) \\ B_{01}(a_0 + \alpha) + e^{-i\phi}B_{00}(a_1 + \beta) \end{pmatrix}, \tag{13}$$

where we have identified  $B_{11} = e^{-i\phi}B_{00}$  and  $B_{10} = B_{01}$ . Considering a vacuum state in the second ingoing beam ( $\beta = 0$ ), we compute the number of photons in the first outgoing beam,

$$\langle n_0^{\text{out}} \rangle = \langle 0, 0 | b_0^\dagger b_0 | 0, 0 \rangle = |\alpha|^2 |B_{00}|^2 = \langle n_0^{\text{in}} \rangle |B_{00}|^2. \tag{14}$$

See that  $\langle n_0^{\text{in}} \rangle = \langle x_0^{\text{in}} \rangle^2$  for  $\alpha \in \mathbb{R}$ , assuming a displacement in the  $x$ -direction, where  $x = \frac{a+a^\dagger}{2}$  is the quadrature operator. Consider that the response of the system is codified in  $\langle n_0^{\text{out}} \rangle$ ; this implies that the measured quantity will be  $\langle n_1^{\text{out}} \rangle = |\alpha|^2 |B_{01}|^2$ .

Having identified the response and the internal variable, we can write the equations of the memristor,

$$\begin{aligned} \langle n_0^{\text{out}} \rangle &= f(\phi, \langle x_0^{\text{in}} \rangle) \langle x_0^{\text{in}} \rangle, \\ \dot{\phi} &= g(\phi, \langle x_0^{\text{in}} \rangle). \end{aligned} \tag{15}$$

Since we have freedom to choose the update of the phase  $\phi$ , we propose a simple function for illustrative purposes,

$$\dot{\phi} = \frac{\omega_0}{\langle x_0^{\text{in}} \rangle_{\text{max}}} \langle x_0^{\text{in}} \rangle. \tag{16}$$

Assuming that we are able to pump the system to induce periodicity in the quadrature of the input state, such that  $\langle x_0^{\text{in}} \rangle = \langle x_0^{\text{in}} \rangle_{\text{max}} \cos \omega t$ , the evolution of  $\phi$  is described by

$$\phi(t) = \phi(0) + \frac{\omega_0}{\omega} \sin \omega t. \tag{17}$$

This implies that

$$\begin{aligned} f(\phi, \langle x_0^{\text{in}} \rangle) &= \langle x_0^{\text{in}} \rangle_{\text{max}} \left[ \cos^2 \frac{\phi(t)}{2} + J_0^4(\Theta) \sin^2 \frac{\phi(t)}{2} \right] \cos \omega t, \\ g(\phi, \langle x_0^{\text{in}} \rangle) &= \omega_0 \cos \omega t. \end{aligned} \tag{18}$$

In Figure 5, we represent  $\langle n_0^{\text{out}} \rangle$  versus  $\langle x_0^{\text{in}} \rangle$  to observe hysteretic behavior, related to that appearing in the  $I$ - $V$  characteristic curve of memristors. The hysteresis loop in this case is pinched, and its area decreases with an increasing frequency of the driving, which means that this system behaves as a memristor in these variables.

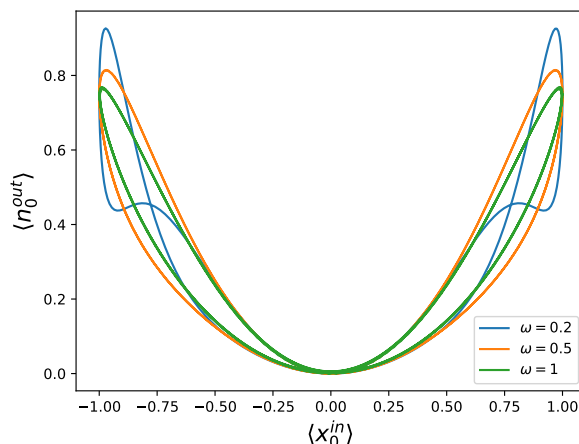


**Figure 5.** Number of photons  $\langle n_0^{\text{out}} \rangle$  of the outgoing beam versus the quadrature of the input state  $\langle x_0^{\text{in}} \rangle$  for coherent states, displaying a pinched hysteresis loop, proving that this system behaves as a memristor. We have plotted this for three different frequencies, namely  $\omega = 0.2$  (blue),  $\omega = 0.5$  (orange), and  $\omega = 1$  (green), exemplifying that the area of the loop decreases for higher frequencies. We have used  $\phi(0) = \frac{\pi}{2}$ ,  $\omega_0 = 1$ , and  $\langle x_0^{\text{in}} \rangle_{\text{max}} = 1$  (see Appendix A for directions of the hysteresis loops).

### 2.2. Squeezed States

It is interesting to study the response of the system when considering squeezed state inputs. Analogous to the displacement operator for coherent states, we can define the squeezing operator  $S(z) = e^{\frac{1}{2}(z a^2 - z^* a^{\dagger 2})}$ , with  $z = r e^{i\varphi}$ , such that a squeezed state is defined as  $|z\rangle = S(z)|0\rangle$ . Using the relation in Equation (10), we can define the transformation

$$S^\dagger(z) a S(z) = a \cosh r - e^{i\varphi} a^\dagger \sinh r. \tag{19}$$

By applying squeezing operators  $S(z_0), S(z_1)$  on the first and second beam, respectively, we obtain

$$\begin{pmatrix} a_0 \\ a_1 \end{pmatrix} \rightarrow \begin{pmatrix} S^\dagger(z_0) a_0 S(z_0) \\ S^\dagger(z_1) a_1 S(z_1) \end{pmatrix} = \begin{pmatrix} a_0 \cosh r_0 - e^{i\varphi_0} a_0^\dagger \sinh r_0 \\ a_1 \cosh r_1 - e^{i\varphi_1} a_1^\dagger \sinh r_1 \end{pmatrix} \tag{20}$$

which represent the inputs to the beam splitter. These modes are modified by the beam splitter as follows,

$$\begin{pmatrix} b_0 \\ b_1 \end{pmatrix}_{\text{squ}} = B(\phi) \begin{pmatrix} a_0 \cosh r_0 - e^{i\varphi_0} a_0^\dagger \sinh r_0 \\ a_1 \cosh r_1 - e^{i\varphi_1} a_1^\dagger \sinh r_1 \end{pmatrix}.$$

We consider a vacuum state in the second ingoing beam ( $r_1 = 0$ ), and compute the number of photons in the first outgoing beam,

$$\langle n_0^{\text{out}} \rangle = \langle 0, 0 | b_0^\dagger b_0 | 0, 0 \rangle = \sinh^2 r_0 |B_{00}|^2 \tag{21}$$

as the response of the system. For the control variable, we choose  $\langle x^2 \rangle = \frac{1}{4} \langle (a + a^\dagger)^2 \rangle$  for the first ingoing beam

$$\langle (x_0^{\text{in}})^2 \rangle = \frac{1}{4} (\cosh^2 r + \sinh^2 r - \sinh 2r \cos \varphi) \tag{22}$$

where we have set  $r_0 = r$  and  $\varphi_0 = \varphi$ . In this setup, our goal is to identify a memristive system satisfying the following equations,

$$\begin{aligned} \langle n_0^{\text{out}} \rangle &= f(\phi, \langle (x_0^{\text{in}})^2 \rangle) \langle (x_0^{\text{in}})^2 \rangle, \\ \dot{\phi} &= g(\phi, \langle (x_0^{\text{in}})^2 \rangle), \end{aligned} \tag{23}$$



with the phase  $\phi$  set as the memory variable, as in the previous section. Fixing the squeezing in the  $x$  axis ( $\varphi = 0$ ), we can write

$$\langle (x_0^{\text{in}})^2 \rangle = \frac{1}{4}(\cosh r - \sinh r)^2, \quad (24)$$

and thus

$$1 - 4\langle (x_0^{\text{in}})^2 \rangle = 2 \sinh r (\cosh r - \sinh r). \quad (25)$$

Then, we find that we can express

$$f(\phi, \langle (x_0^{\text{in}})^2 \rangle) = \left[ \frac{1 - 4\langle (x_0^{\text{in}})^2 \rangle}{4\langle (x_0^{\text{in}})^2 \rangle} \right]^2 |B_{00}|^2. \quad (26)$$

The number of photons measured in the outgoing beam corresponding to the environment is given by

$$\langle n_1^{\text{out}} \rangle = 16 \left[ \frac{x_0^2 - \langle (x_0^{\text{in}})^2 \rangle}{\langle (x_0^{\text{in}})^2 \rangle} \right]^2 |B_{01}|^2 \langle (x_0^{\text{in}})^2 \rangle, \quad (27)$$

from which  $\langle (x_0^{\text{in}})^2 \rangle$  can be obtained. As the update of the memory variable, we propose the function

$$\phi = \pm \frac{\omega_0}{x_0} \sqrt{x_0^2 - \langle (x_0^{\text{in}})^2 \rangle}, \quad (28)$$

where  $x_0^2 = \langle (x_0^{\text{in}})^2 \rangle_{\text{vac}} = 1/4$ . Assuming we are able to engineer a periodic pumping  $\langle (x_0^{\text{in}})^2 \rangle = (1 - \alpha \cos^2 \omega t)/4$  for the input states, we have that

$$g(\phi, \langle (x_0^{\text{in}})^2 \rangle) = \pm \omega_0 \sqrt{\alpha} \cos \omega t, \quad (29)$$

leading to the evolution of  $\phi$  to be given by

$$\phi(t) = \phi(0) + \frac{\omega_0}{\omega} \sqrt{\alpha} \sin \omega t. \quad (30)$$

We can observe hysteresis loops when representing the number of photons in the first outgoing beam versus  $\langle x^2 \rangle$  in the input beam, as can be seen in Figure 6.

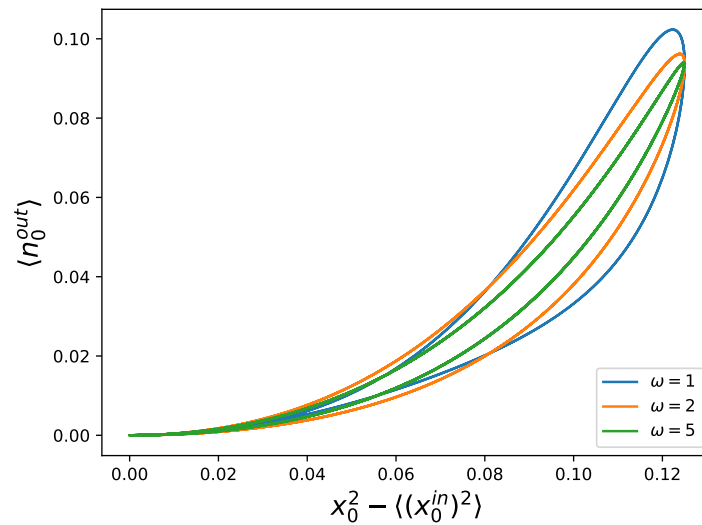


**Figure 6.** Number of photons  $\langle n_0^{\text{out}} \rangle$  of the outgoing beam versus the second-moment of the quadrature of the input state  $\langle (x_0^{\text{in}})^2 \rangle$  for squeezed states, displaying a pinched hysteresis loop, proving that this system behaves as a memristor. We have plotted this for three different frequencies, namely  $\omega = 1$  (blue),  $\omega = 2$  (orange), and  $\omega = 5$  (green), exemplifying that the area of the loop decreases for higher frequencies. We have used  $\phi(0) = \frac{\pi}{2}$ ,  $\omega_0 = 5$ ,  $\alpha = 0.5$ , and  $x_0 = 1/4$  (see Appendix A for directions of the hysteresis loops).

### 2.3. Fock States

In this category, several one- and two-photon Fock states can be considered, such as

$$\begin{aligned}
 |\psi_1\rangle &= \alpha|1_{\omega_0}, 0_{\omega_1}\rangle + \beta|0_{\omega_0}, 1_{\omega_1}\rangle = (\alpha a_{\omega_0}^\dagger + \beta a_{\omega_1}^\dagger)|0, 0\rangle, \\
 |\psi_2\rangle &= |1_{\omega_0}, 1_{\omega_1}\rangle = a_{\omega_0}^\dagger a_{\omega_1}^\dagger |0, 0\rangle, \\
 |\psi_3\rangle &= |2_{\omega_0}, 0_{\omega_1}\rangle = \frac{1}{\sqrt{2}}(a_{\omega_0}^\dagger)^2 |0, 0\rangle, \\
 |\psi_4\rangle &= |0_{\omega_0}, 2_{\omega_1}\rangle = \frac{1}{\sqrt{2}}(a_{\omega_1}^\dagger)^2 |0, 0\rangle.
 \end{aligned} \tag{31}$$

The only Fock input state, among the ones given above, that allows for a change in the control over the timescale of the feedback mechanism is the first one,  $|\psi_1\rangle$ . We begin from this state and compute the number of photons in the outgoing beam,

$$\langle n_0^{\text{out}} \rangle_{\psi_1} = \langle \psi_1 | b_0^\dagger b_0 | \psi_1 \rangle = \langle \psi_1 | (\bar{B}_{00} a_0^\dagger + \bar{B}_{01} a_1^\dagger) (B_{00} a_0 + B_{01} a_1) | \psi_1 \rangle, \tag{32}$$

and choose  $\alpha = \cos \omega t$  and  $\beta = \sin \omega t$  to obtain

$$\langle n_0^{\text{out}} \rangle_{\psi_1} = \cos^2 \omega t \cos^2 \frac{\phi}{2} + (c_1 \cos \omega t + 2c_2 \sin \omega t)^2 \sin^2 \frac{\phi}{2}, \tag{33}$$

where  $c_1 = J_0^2(\Theta)$  and  $c_2 = \sum_{k=1}^\infty J_k(\Theta) J_{k-1}(\Theta)$ . The number of photons dissipated to the environment is then

$$\langle n_1^{\text{out}} \rangle_{\psi_1} = \sin^2 \omega t \cos^2 \frac{\phi}{2} + (c_1 \sin \omega t + 2c_2 \cos \omega t)^2 \sin^2 \frac{\phi}{2}. \tag{34}$$

From these measurements,  $\alpha$  can be inferred to design the following update of the memory variable,

$$\dot{\phi} = \omega_0 \alpha = \omega_0 \cos \omega t, \tag{35}$$

such that its time evolution is described by

$$\phi(t) = \phi(0) + \frac{\omega_0}{\omega} \sin \omega t. \quad (36)$$

In Figure 7, we plot the output photon number against  $\alpha$ , which represents the square root of the average photon number in the first ingoing beam,

$$\langle n_0^{\text{in}} \rangle_{\psi_1} = \langle \psi_1 | a_0^\dagger a_0 | \psi_1 \rangle = |\alpha|^2. \quad (37)$$

We obtain hysteretic behavior in the system, but the loops cross at a point that is moving with the frequency  $\omega$  of the driving, approaching zero for higher frequencies, and the area of the loops does not seem to decrease with increasing frequency. Since the system and the environment are entangled, this system does not represent a memristor.

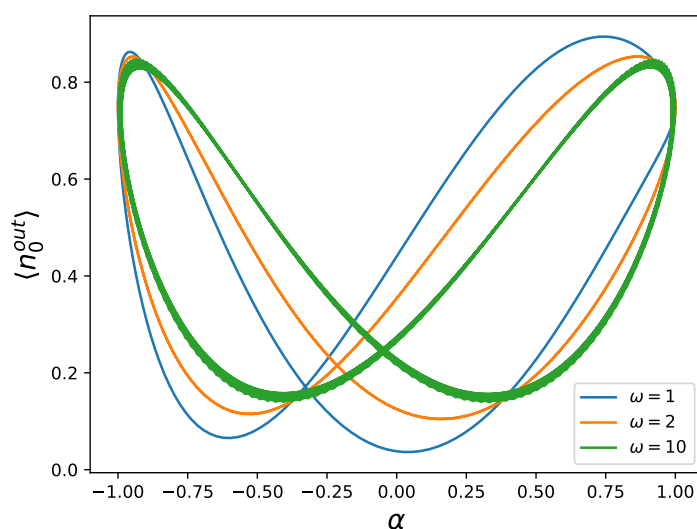


**Figure 7.** Number of photons  $\langle n_0^{\text{out}} \rangle$  of the outgoing beam versus  $\alpha = \cos \omega t$  for a frequency-superposition Fock state, displaying a pinched hysteresis loop, where the point of crossing approaches zero with higher  $\omega$ . This system does not behave as a memristor. We have plotted this for three different frequencies, namely  $\omega = 1$  (blue),  $\omega = 2$  (orange), and  $\omega = 10$  (green), exemplifying that the area of the loop does not seem to decrease for higher frequencies. We have used  $\phi(0) = \frac{\pi}{2}$ , and  $\omega_0 = 1$  (see Appendix A for directions of the hysteresis loops).

### 3. Discussion

We have followed a scheme to build a resistive memory element in a quantum platform. We have reproduced this behavior in quantum photonics with frequency-codified quantum states, by engineering a frequency mixer as a tunable beam splitter with a measurement scheme that modifies its reflectivity through classical feedback. Hysteretic behavior was found when representing the response of the system versus the control, a sign of memristive systems. To form a network, these beamsplitters need to be connected using the output of one as the input for the next. The behavior of such a device under quantum state inputs needs to be studied in order to test the viability of a quantum neural network constructed in this quantum photonics platform. Such a result could represent a direct hardware-based implementation of quantum machine learning algorithms.

In this study, we focused on a frequency-bin memristor design that is feasible. The tunable beam splitter outlined in Figure 2 and expressed by Equation (5) was experimentally demonstrated with behavior matching theory extremely well [20,29]. Nevertheless, practical limitations present challenges toward realizing this memristor's full potential in the laboratory. For example, in the tabletop demonstrations of the frequency beam splitter thus far, component insertion losses have led

to overall throughputs of  $\sim 5\%$ —a significant limitation, particularly for continuous-variable encoding, and much lower than the  $\mathcal{P} = 97.6\%$  indicated in the lossless theory. Nonetheless, unlike the success probability  $\mathcal{P}$ , insertion losses stem from nonidealities (e.g., mode mismatch and waveguide loss) that can in principle be eliminated through device engineering. In fact, integrated microring-based pulse shapers [31] from existing foundries, coupled with ultralow-loss EOMs [32], provide a promising outlook for chip-scale frequency memristors with markedly lower loss.

Additionally, our memristor design relies heavily on real-time feedback of the phase shift  $\phi$ . Ideally, given mode separation  $\Delta\nu \approx 25$  GHz, one would like update speeds in the  $\sim$ ns regime—fast, but sufficiently slower than the RF period, in order to retain the validity of the frequency-bin model. Such refresh rates are beyond the bandwidths of liquid-crystal-on-silicon pulse shaper technology [33], but would be readily attainable with phase shifters utilizing the electro-optic effect, a natural choice for on-chip pulse shapers based on microring modulators. Thus, moving on chip should not only improve efficiency, but also enable the update speeds desired for memristor feedback.

Memory effects are not an exclusive feature of quantum dynamics, being also present in classical physics. Our understanding regarding quantum non-Markovian behavior has markedly increased in the last few years [34–36]. Therefore, moving forward with this design, the question regarding the quantumness of the time correlations generated in the output beam should be experimentally addressed by a measure of quantum non-Markovianity or by means of a Leggett–Garg inequality [37]. Interestingly, these two concepts are deeply linked [38].

As demonstrated by our results, a memristor can be practically implemented in a photonic system with frequency-encoded optical fields, thus providing a novel platform for the development of quantum circuits for simulating complex quantum systems, where the characteristic non-linear behavior of the memristor can play a major role.

**Author Contributions:** Conceptualization, M.S.; Methodology, T.G.-R., J.M.L., and L.C.C.; Software, T.G.-R.; Writing—original draft, T.G.-R.; and Writing—review and editing, J.M.L., L.C.C., and M.S. All authors have read and agreed to the published version of the manuscript.

**Funding:** The authors acknowledge support from Spanish Government PGC2018-095113-B-I00 (MCIU/AEI/FEDER, UE) and Basque Government IT986-16. The authors also acknowledge support from the projects QMiCS (820505) and OpenSuperQ (820363) of the EU Flagship on Quantum Technologies, as well as the EU FET Open Grant QuomorphiC. This work was supported by the U.S. Department of Energy, Office of Science, Office of Advanced Scientific Computing Research (ASCR) quantum algorithm teams program, under field work proposal number ERKJ333. LCC would like to acknowledge the financial support from the Brazilian ministries MEC and MCTIC, funding agency CNPq, and the Brazilian National Institute of Science and Technology of Quantum Information (INCT-IQ). This study was financed in part by the Coordenação de Aperfeiçoamento de Pessoal de Nível Superior—Brasil (CAPES)—Finance Code 001. A portion of this work was performed at Oak Ridge National Laboratory, managed by UT-Battelle, LLC, for the US Department of Energy under contract No. DE-AC05-00OR22725.

**Acknowledgments:** The authors are grateful to Pavel Lougovski and Enrique Solano for helpful discussions.

**Conflicts of Interest:** The authors declare no conflict of interest.

## Appendix A. Direction of Hysteresis

In this section, we introduce the hysteresis plots that are discussed above, and we show the direction of the evolution of the hysteresis loops. In Figure A1, we plot the hysteresis loops for the different input states, and the different driving frequencies considered. Figure A1a–c shows coherent states (from Figure 5); Figure A1d–f represents squeezed states (from Figure 6); and Figure A1g–i shows Fock states (from Figure 7). The digits in Figure A1d–f show the order of the arrows in the hysteresis loop. Since the control variable chosen for squeezed states is  $x_0^2 - \langle (x_0^{\text{in}})^2 \rangle = (\alpha/4) \cos^2 \omega t$ , the hysteresis loop is only displayed on the first quadrant. This function will behave as an absolute value, and the direction needs to be specified.

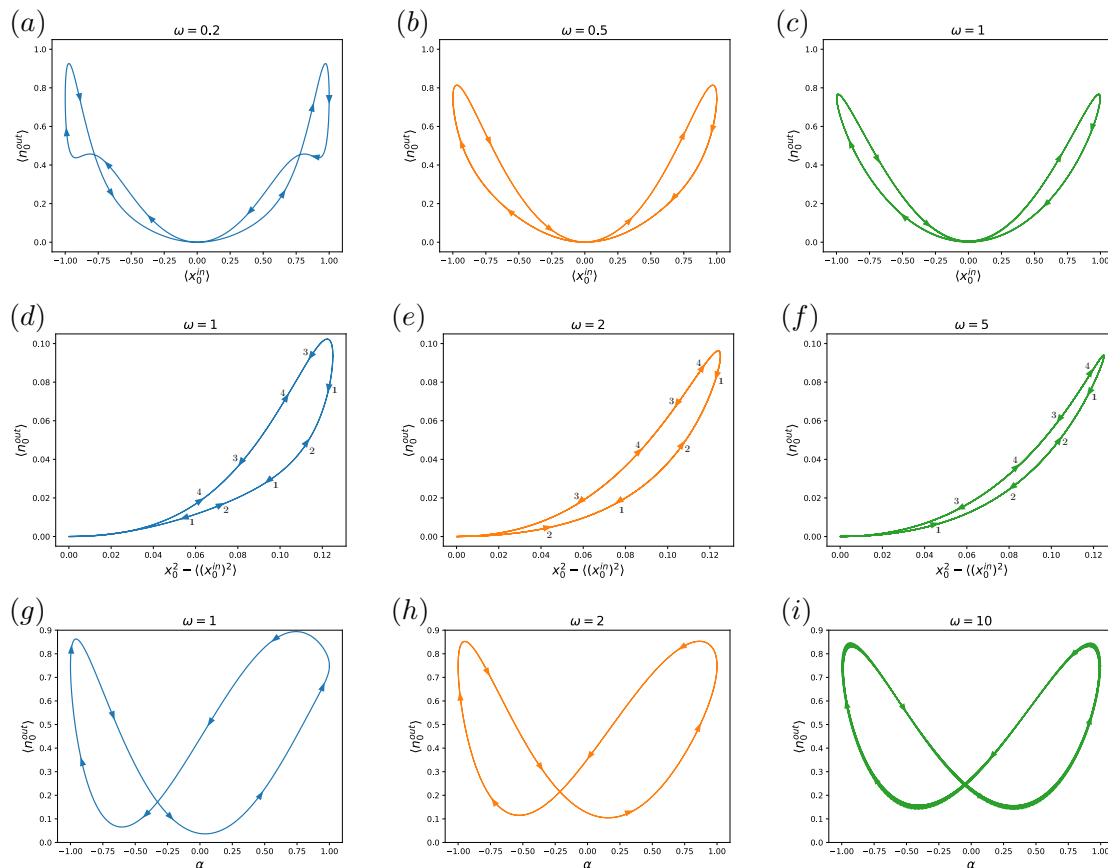


**Figure A1.** Number of photons  $\langle n_0^{\text{out}} \rangle$  of the outgoing beam versus the corresponding control variable for coherent, squeezed, and Fock state inputs, for different driving frequencies: (a–c) coherent states; (d–f) squeezed states; and (g–i) Fock states. Since the control is always positive for squeezed states, we introduce a number to illustrate the order of the arrows in the hysteresis plots.

## References

- Snider, G.; Amerson, R.; Carter, D.; Abdalla, H.; Qureshi, M.S.; Léveillé, J.; Versace, M.; Ames, H.; Patrick, S.; Chandler, B.; et al. From synapses to circuitry: Using memristive memory to explore the electronic brain. *Computer* **2011**, *44*, 21. [[CrossRef](#)]
- Pershin, Y.V.; di Ventra, M. Neuromorphic, Digital, and Quantum Computation with Memory Circuit Elements. *Proc. IEEE* **2012**, *100*, 2071. [[CrossRef](#)]
- Cohen, G.Z.; Pershin, Y.V.; di Ventra, M. Lagrange Formalism of Memory Circuit Elements: Classical and Quantum Formulation. *Phys. Rev. B* **2012**, *85*, 165428. [[CrossRef](#)]
- Biolek, Z.; Biolek, D. Euler-Lagrange Equations of Networks with Higher-Order Elements. *Radioengineering* **2017**, *26*, 2. [[CrossRef](#)]
- Jeltsema, D.; Doria-Cerezo, A. Port-Hamiltonian Formulation of Systems with Memory. *Proc. IEEE* **2012**, *100*, 6. [[CrossRef](#)]
- Caravelli, F.; Carbajal, J.P. Memristors for the Curious Outsiders. *Technologies* **2018**, *6*, 118. [[CrossRef](#)]
- Salmilehto, J.; Deppe, F.; di Ventra, M.; Sanz, M.; Solano, E. Quantum Memristors with Superconducting Circuits. *Sci. Rep.* **2017**, *7*, 42044. [[CrossRef](#)]
- Kubo, R. Statistical-mechanical theory of irreversible processes. I. General theory and simple applications to magnetic and conduction problems. *J. Phys. Soc. Jpn.* **1957**, *12*, 570. [[CrossRef](#)]
- Chua, L.O. Memristor-The missing circuit element. *IEEE Trans. Circuit Theory* **1971**, *18*, 507. [[CrossRef](#)]
- Strukov, D.B.; Snider, G.S.; Stewart, D.R.; Williams, R.S. The missing memristor found. *Nature* **2008**, *453*, 80. [[CrossRef](#)]
- Miranda, E.; Jiménez, D.; Suñé, J. The Quantum Point-Contact Memristor. *IEEE Electron Dev. Lett.* **2012**, *33*, 10. [[CrossRef](#)]

12. Barrios, G.A.; Retamal, J.C.; Solano, E.; Sanz, M. Analog simulator of integro-differential equations with classical memristors. *Sci. Rep.* **2019**, *9*, 12928. [[CrossRef](#)]
13. Jeong, D.S.; Kim, K.M.; Choi, B.J.; Hwang, C.S. Memristors for energy-efficient new computing paradigms. *Adv. Electron. Mater.* **2016**, *2*, 1600090. [[CrossRef](#)]
14. Silva, F.; Sanz, M.; Seixas, J.; Solano, E.; Omar, Y. Perceptrons from Memristors. *Neural Netw.* **2019**, *122*, 273. [[CrossRef](#)]
15. Huang, A.; Zhang, X.; Li, R.; Chi, Y. *Memristor Neural Network Design*; IntechOpen: London, UK, 2018; pp. 249–281. [[CrossRef](#)]
16. Hodgkin, A.L.; Huxley, A.F. A quantitative description of membrane current and its application to conduction and excitation in nerve. *J. Physiol.* **1952**, *117*, 500.
17. Chua, L.O.; Sbitnev, V.; Kim, H. Hodgkin-Huxley axon is made of memristors. *Int. J. Bifurc. Chaos* **2012**, *22*, 1230011. [[CrossRef](#)]
18. Pfeiffer, P.; Egusquiza, I.L.; di Ventra, M.; Sanz, M.; Solano, E. Quantum Memristor. *Sci. Rep.* **2016**, *6*, 29507. [[CrossRef](#)]
19. Sanz, M.; Lamata, L.; Solano, E. Quantum Memristors in Quantum Photonics. *APL Photonics* **2018**, *3*, 080801. [[CrossRef](#)]
20. Lu, H.-H.; Lukens, J.M.; Peters, N.A.; Odele, O.D.; Leaird, D.E.; Weiner, A.M.; Lougovski, P. Electro-Optic Frequency Beam Splitters and Tritters for High-Fidelity Photonic Quantum Information Processing. *Phys. Rev. Lett.* **2018**, *120*, 030502. [[CrossRef](#)]
21. Schuld, M.; Sinayskiy, I.; Petruccione, F. An introduction to quantum machine learning. *Contemp. Phys.* **2015**, *56*, 172. [[CrossRef](#)]
22. Biamonte, J.; Wittek, P.; Pancotti, N.; Rebentrost, P.; Wiebe, N.; Lloyd, S. Quantum Machine Learning. *Nature* **2017**, *549*, 195. [[CrossRef](#)]
23. Lukens, J.M.; Lougovski, P. Frequency-encoded photonic qubits for scalable quantum information processing. *Optica* **2017**, *4*, 8. [[CrossRef](#)]
24. Menicucci, N.C.; Flammia, S.T.; Pfister, O. One-Way Quantum Computing in the Optical Frequency Comb. *Phys. Rev. Lett.* **2008**, *101*, 130501. [[CrossRef](#)]
25. Kues, M.; Reimer, C.; Lukens, J.M.; Munro, W.J.; Weiner, A.M.; Moss, D.J.; Morandotti, R. Quantum optical microcombs. *Nat. Photon.* **2019**, *13*, 170. [[CrossRef](#)]
26. Kobayashi, T.; Ikuta, R.; Yasui, S.; Miki, S.; Yamashita, T.; Terai, H.; Yamamoto, T.; Koashi, M.; Imoto, N. Frequency-domain Hong–Ou–Mandel interference. *Nat. Photon.* **2016**, *10*, 441. [[CrossRef](#)]
27. Clemmen, S.; Farsi, A.; Ramelow, S.; Gaeta, A.L. Ramsey Interference with Single Photons. *Phys. Rev. Lett.* **2016**, *117*, 223601. [[CrossRef](#)]
28. Lu, H.-H.; Weiner, A.M.; Lougovski, P. Quantum Information Processing with Frequency-Comb Qudits. *IEEE Photon. Technol. Lett.* **2019**, *31*, 1858. [[CrossRef](#)]
29. Lu, H.-H.; Lukens, J.M.; Peters, N.A.; Peters, N.A.; Weiner, A.M.; Lougovski, P. Quantum interference and correlation control of frequency-bin qubits. *Optica* **2018**, *5*, 1455. [[CrossRef](#)]
30. di Ventra, M.; Pershin, Y.V. On the physical properties of memristive, memcapacitive and meminductive systems. *Nanotechnology* **2013**, *24*, 255201. [[CrossRef](#)]
31. Wang, J.; Shen, H.; Fan, L.; Wui, R.; Niu, B.; Varghese, L.T.; Xuan, Y.; Leaird, D.E.; Wang, X.; Gan, F.; et al. Reconfigurable radio-frequency arbitrary waveforms synthesized in a silicon photonic chip. *Nat. Commun.* **2015**, *6*, 5957. [[CrossRef](#)]
32. Wang, C.; Zhang, M.; Chen, X.; Bertrand, M.; Shams-Ansari, A.; Chandrasekhar, S.; Winzer, P.; Lončar, M. Integrated lithium niobate electro-optic modulators operating at CMOS-compatible voltages. *Nature* **2018**, *562*, 101. [[CrossRef](#)]
33. Roelens, M.A.F.; Frisken, S.; Bolger, J.A.; Abakoumov, D.; Baxter, G.; Poole, S.; Eggleton, B.J. Dispersion trimming in a reconfigurable wavelength selective switch. *J. Lightw. Technol.* **2008**, *26*, 73. [[CrossRef](#)]
34. Capela, M.; Céleri, L.C.; Modi, K.; Chaves, R. Monogamy of Temporal Correlations: Witnessing non-Markovianity Beyond Data Processing. *arXiv* **2019**, arXiv:1910.04236. [[CrossRef](#)]
35. Pollock, F.A.; Rodríguez-Rosario, C.; Frauenheim, T.; Paternostro, M.; Modi, K. Operational Markov Condition for Quantum Processes. *Phys. Rev. Lett.* **2018**, *120*, 040405.
36. Milz, S.; Kim, M.S.; Pollock, F.A.; Modi, K. Completely Positive Divisibility Does Not Mean Markovianity. *Phys. Rev. Lett.* **2019**, *123*, 040401. [[CrossRef](#)] [[PubMed](#)]

37. Leggett, A.J.; Garg, A. Quantum mechanics versus macroscopic realism: Is the flux there when nobody looks? *Phys. Rev. Lett.* **1985**, *54*, 857. [[CrossRef](#)] [[PubMed](#)]
38. Souza, A.M.; Li, J.; Soares-Pinto, D.O.; Sarthour, R.S.; Oliveira, S.; Huelga, S.F.; Paternostro, M.; Semião, F.L. Experimental Demonstration of non-Markovian Dynamics via a Temporal Bell-like Inequality. *arXiv* **2013**, arXiv:1308.5761. [[CrossRef](#)]



© 2020 by the authors. Licensee MDPI, Basel, Switzerland. This article is an open access article distributed under the terms and conditions of the Creative Commons Attribution (CC BY) license (<http://creativecommons.org/licenses/by/4.0/>).